Atomic and vibrational origins of mechanical toughness in bioactive cement during setting

Kun V. Tian[1], Bin Yang[2,3], Yuan-Zheng Yue[4,5], Daniel T. Bowron[6], Jerry Mayers[6], Robert S. Donnan[3], Csaba Dobó-Nagy[1], John W. Nicholson[7], De-Cai Fang[8], A. Lindsay Greer[9], Gregory A. Chass[10] & G. Neville Greaves[4,9,11]

[1]Materials Science Research Institute, Faculty of Dentistry, Semmelweis University, Budapest 1088, Hungary

[2]Department of Electronic and Electrical Engineering, University of Chester, Thornton Science Park, Chester CH2 4NU UK.

[3]School of Electronic Engineering and Computer Science, Queen Mary University of London, London E1 4NS, United Kingdom

[4]State Key Laboratory of Silicate Materials for Architectures, Wuhan University of Technology, Wuhan 430070, China

[5]Department of Chemistry and Bioscience, Aalborg University, DK-9220 Aalborg, Denmark

[6]ISIS Facility, STFC Rutherford Appleton Laboratory, Chilton, Didcot, Oxon OX11 0QX, United Kingdom

[7]School of Sport, Health and Applied Science, St. Mary's University College, London TW1 4SX, United Kingdom

[8]Key Laboratory of Theoretical and Computational Photochemistry, Ministry of Education, College of Chemistry, Beijing Normal University, Beijing, 100875, China

[9]Department of Materials Science & Metallurgy, University of Cambridge, 27 Charles Babbage Road, Cambridge CB3 0FS, United Kingdom

[10]School of Biological and Chemical Sciences, Queen Mary University of London, London E1 4NS, United Kingdom

[11]Institute of Mathematics, Physics and Computer Science, Aberystwyth University, Aberystwyth SY23 3BZ, United Kingdom

Correspondence and requests for materials should be addressed to G.A.C. (email: g.chass@qmul.ac.uk) and G.N.G. (email: gng25@cam.ac.uk)

Bioactive glass-ionomer cements (GICs) have been in widespread use for ~40 years in dentistry and medicine. However, these composites fall short of the toughness needed for permanent implants. Significant impediment to improvement has been the requisite use of conventional destructive mechanical testing, which is necessarily retrospective. Herein we show quantitatively, through the novel use of calorimetry, terahertz spectroscopy, and neutron scattering, how GIC's developing fracture toughness during setting is related to interfacial THz-dynamics, changing atomic cohesion, and fluctuating interfacial configurations. Contrary to convention, we find setting is non-monotonic, characterised by abrupt features not previously detected, including a glass-polymer coupling point, an early setting point, where decreasing toughness unexpectedly recovers, followed by stress-induced weakening of interfaces. Subsequently, toughness declines asymptotically to long-term fracture test values. We expect the insight afforded by these *in situ* non-destructive techniques will assist in raising understanding of the setting mechanisms and associated dynamics of cementitious materials.

(abstract is now 150 words)

Worldwide demand for durable biomaterials emanates from population aging and from emergent developing countries. Historically, implanting foreign materials into the body has been dentistry-led. The optimisation of tooth replacements remains incomplete, however, problems stemming from conflicts between mechanical toughness, biocompatibility, adhesion and appearance. For commonly used mercury-silver amalgams, this is compounded by toxicity and disposal. The United Nations Environment Programme (UNEP) assesses mercury to be "a global threat to human and environmental health," listing amalgams as a source[1]. With 125 million amalgam restorations carried out annually in Europe, the European Commission advocates atraumatic restorative treatment using mercury-free alternatives[2], highlighting glass-

ionomer cements (GICs) (Figure 1a) as an excellent option. Developed over 40 years[3–8] GICs are the product of a basic fluoro-phospho-alumino-silicate glass powder and an aqueous poly(acrylic) acid (PAA) solution (Figure 1b, Methods) – glass polyalkenoate cements[9]. Although cost-effective and environmentally friendly[2], caries-resistant and bioactively mineralising dentine[10,11], GICs remain too brittle for permanent implants[12,13]. With exceptional bonding to the apatite phase of bone, GICs have also been considered for other aspects of surgery[14–16], but necessarily confined to non-load-bearing applications with moderate durability requirements[17].

Damage tolerance is assessed through fracture toughness K_C and yield strength σ_Y, both traditionally measured by destructive methods[18]. Average values for dental materials and their components have been collated to create Figure 1c. This log K_C versus log σ_Y plot follows the Ashby scheme[19] widely used elsewhere in mechanics to categorise conflicts between strength and toughness in composite materials[20]. Polymers and ceramics lie in the lower half with K_C values greater than 1 MPa $m^{1/2}$; brittle materials like glasses have K_C values less than this. Indeed the yield strength σ_Y of glassy materials covers many decades[21] from ~10 GPa (glass fibres) to ~1 MPa (pre-damaged glass). Respective K_C and σ_Y values of GICs cluster around those of dentine and amalgam, but clearly have less toughness and strength than either.

For composites in general, and GICs in particular, K_C and σ_Y develop during setting, starting out as highly deformable and incompressible slurries which subsequently harden to form rigid, inflexible cements. The compressibility κ relates directly to the shape of the interatomic potentials of a given system[22]. The narrower and deeper the potential is, the stronger and more rigid the atomic cohesion and *vice versa*. More rigid materials have a higher shear modulus G and lower κ, but most importantly tend to have a higher $G.\kappa$, and to be brittle. In particular,

Poisson's ratio ν[22], a function of $G.\kappa$, sharply differentiates between brittleness and ductility. If toughness is converted to fracture energy G_C[23], as a function of ν, this forms a clear sigmoid, with an inflection point (at $\nu \approx 0.33$)[24] separating ductile ($\nu >$ ~0.33) from brittle ($\nu <$ ~0.33) materials (Figure 1d). Originally discovered for metals[24], this important empirical relationship also holds for inorganic glasses and polymers, the ingredients of GICs, and other non-metals. All these materials have been incorporated into Figure 1d to create a guide for assessing the extent of brittleness of dental materials. In particular, as setting advances, ν must decrease significantly, from $\nu \approx 0.5$, when the cement is a virtually incompressible liquid to $\nu <$ ~0.33, as it solidifies into a brittle solid. This is illustrated by the dashed arrow for GICs, which finally become too brittle, with $\nu \approx 0.30$[25] compared with amalgam with $\nu \approx 0.34$[22,55]. The ultimate aim is to modify GICs so that they are closer in toughness to amalgam and dentin.

The initial setting mechanism of GICs is an acid-base reaction between the aqueous PAA and the glass component (Figure1b, Methods)[3,4]. As with alumina-silicate glasses, water corrosion ruptures bridging-oxygens (BOs) to form SiOH[26] and AlOH[27] groups, initially creating an aqueous gel at the glass surface. For the G338 glass used in GICs, PO_4^- and F^- will also be released, along with Na^+ cations, freeing Al^{3+} and Ca^{2+} cations to cross-link the polymer to form a strong polysalt matrix[4,5]. Aluminium-chelation by the polymer drives the conversion of Al(IV) tetrahedra to higher-coordinated sites[28] at the interfaces between glass and matrix as well as those between cross-linked polymer chains within the matrix. Higher-coordinated sites include both pyramidal Al(V) as well as octahedral Al(VI) geometries. Similar changes in interfacial configuration in proteins, for example, are manifested by variations of orientation-dependent dynamics in the sub-THz range[29]. These low-frequency modes are known to modulate mechanical[30], optical[31] and biophysical properties[32] of macromolecular systems.

We have therefore turned to non-destructive techniques that record changing atomic structures, associated collective sub-THz dynamics and atomic-cohesion during the first 3 days of setting, uncovering highly non-linear behaviour over various stages, and providing indications of the sources of eventual brittleness and low strength.

To make our extended *in situ* experiments relevant to current dental practice, we have chosen the commercial G338 ionomer glass (Figure 1b), in regular use since the early 1980s. To ensure practical relevance, we employed standard clinical preparatory mixing to examine setting from the polymer-glass mixture to the hardened cement The heterogeneous glass powder has been imaged by transmission electron microscopy (TEM) and exhibits significant heterogeneity, with three glass phases identifiable on the scale of 5 to 50 nm (Figure 2a). Figure 2b and Supplementary Figure 1 show the isobaric heat capacity C_p of both G338 and GIC samples as a function of temperature determined by differential scanning calorimetry (DSC). The C_p of fresh G338 sample (red curve) exhibits the effects of water loss, after which (blue curve) three sharp glass transitions can be deciphered. Following 62 hours of setting the C_p of the GIC (green curve) demonstrates the evolution of the glass-transition regions of the remaining glass.
Coherent terahertz spectroscopy (CTS)[33] has been employed to track changes in inter-particle binding at the interfaces through variations in collective low-frequency atomic dynamics during setting. Non-monotonic behaviour is clearly evident, revealing several large swings in the magnitude of THz dynamics (Figure 2c).

For observing mechanical toughness K_C atomically, we have turned to *in situ* neutron Compton scattering (NCS)[34], where neutron momentum recoil Δp measures the atomic cohesion. The development of Δp during setting at 300 K is clearly oscillatory (Figure 3a, Supplementary Figure 2). Using a new empirical relationship between the momentum recoil Δp values and

published fracture toughness values (Figure 3b), changes in atomic K_C have been analysed both for the total system K_C^{av} (Figure 3c,d) and for separate elements $K_C^{H,F,O,Al}$ (Figure 3e,f)

In situ neutron-scattering measurements also reveal complementary variations in the structure factor $S(Q)$[35] associated with nanoscopic structure changes taking place during setting (Figure 4a,c), and in the real-space transform $G(r)$ (Figure 4b,d,e). This extensive set of *in situ* experiments has been used to quantify mechanical, structural and dynamical parameters during the setting of GICs, previously unobtainable atomistically[7].

Results

Heterogeneous glass. The G338 glass is chemically complex, containing ingredients for cementation (calcium, phosphate and alumino-silicate), mineralisation (phosphate and fluoride), dental-caries resistance (fluoride), and opal appearance (Ca+F – rich particles). The network forming ions are Si^{4+}, P^{5+}, with the majority being Al^{3+}. Al^{3+} can be charge-compensated for tetrahedral configuration by P^{5+}, and also by Na^+ and Ca^{2+} which, as network-modifiers, can promote the formation of non-bridging oxygens (NBO) within the bridging oxygen (BO) alumina-silicate network[4,36]. Considerable fluorine content further depolymerises the glass melt, leading to low liquidus temperatures[28]. In the glass, Al^{3+} coordinates both to BOs and F^-[36], while F^- complexes with Ca^{2+} and Na^+ as well as with Al^{3+}. SiO_4 and PO_4 tetrahedra principally link via BOs to Al polyhedra, and, while these are mainly tetrahedral, Al(V) and Al(VI) configurations also occur, particularly at the developing interfaces, with the proportions changing during cement setting[28,36].

The as-received G338 glass powder (Methods) comprises micron-sized particles (Figure 2a) exhibiting extensive amorphous phase-separation, as others have reported[17,37]. Our high-

resolution TEM image includes a continuous matrix (GP_1), in which are embedded 30–50 nm spherical rosette domains (GP_2), decorated by 5–10 nm droplets (GP_3). GP_2 and GP_3 are highlighted by large and small dashed circles respectively, and are generally seen throughout this image and those of other particles. All three glass phases (GPs) are neutron-amorphous (Figure 4a) and the three glassy states can be verified by DSC traces (Figure 2b). These reveal three glass transitions: T_{g1} (701 K), T_{g2} (732 K) and T_{g3} (782 K). The small size of glass phases and overlaying within TEM images prevents measurement of phase compositions to correlate with T_gs. However, as amorphous phase separation is the primary source for bulk crystalline nucleation in glass ceramics[38], crystallographic studies of dental ceramics and devitrified GIC glasses[37] identify possible glass-phase compositions. In particular, G338 glass, which is a typical phosphate-containing fluoro-alumino-silicate glass, exhibits amorphous phase separation resembling the morphology in Figure 2a and at least two glass transitions at similar temperatures to those appearing in Figure 2b[37]. Further annealing drives crystallisation by bulk nucleation to a fluoro-phosphate phase and an alumino-silicate phase, the former emanating from amorphous phase-separated droplets and the latter from the surrounding matrix[37,39]. Accordingly we attribute the surrounding matrix seen in our TEM images to an alumino-silicate glass phase (GP1 T_{g1}) and the nanophase droplets to a Ca-F-P-rich glass phase (GP3 T_{g3}). From the glass composition (Methods, Materials) the remaining 30–50 nm spherical domains suggest a Ca-F-rich glass phase (GP2 T_{g2}). These attributions to the phase separated components have been confirmed in a recent parallel study[40].

Thermodynamically, the as-received G338 glass is far from equilibrium, as evidenced by the broad exothermic peak around 720 K that precedes the glass transitions (Figure 2b red curve). This shows the release of the enthalpy trapped during the very rapid quenching of the G338 melt[41] and is absent on reheating (Figure 2b blue curve). Accordingly, we expect each of the three separated amorphous phases GP_1, GP_2 and GP_3 (Figure 2a) to be structurally and

energetically heterogeneous in the as-received glass, as discovered in other hyperquenched glasses[41]. Unstable phases will help drive the hydration process when PAA and glass are mixed.

By heating the GIC cement above room temperature, DSC reveals, first the release of water and any organic impurities, then the decomposition of the polymer which coincides with the three T_gs in the annealed glass (Supplementary Figure 1a). The physical consequences of GIC setting are reflected in the altered glass-transition pattern of the residual glass (Figure 2b green curve) compared with the annealed G388 glass (Figure 2b blue curve). Most obviously, the boundaries between all three glass transitions in the GIC cement are less distinct, suggesting that all the phases have reacted with PAA. This is most pronounced for GP2 T_{g2} and GP3 T_{g3}, where the jump from glass to liquid is reduced, which will be partly due to their large surface area. Reactions with PAA might promote a disorder-order transition[41], or even partial mineralisation, both of which would lower the glass-transition peaks. By contrast, the onset temperature of GP1 T_{g1} is least affected by setting, indicating that the primary alumino-silicate network remains largely intact during setting.

Cooperative interfacial dynamics. We observe time-dependent changes in the sub-THz range using CTS[33] in the early stages as GIC cementation advances (Figure 2c). These occur between the separate CTS values of the glass and polymer. Since bulk values will not vary, the changes that we see must relate directly to the low-frequency dynamics developing at the interfaces between glass and polymer as well as those between cross-linked polymer chains within the matrix during setting. The vibrational modes in the sub-THz energy are centred around 0.5 THz and mainly involve collective motions of constituent atoms. These will be increasingly added to, during setting, by inter-component librational changes such as twisting, bending and flexing, with interfacial links serving as pivot-points. As these encompassing motions modulate macroscopic interfacial and mechanical properties[29,30,32], such as plasticity and elasticity[31], the

initial dip in CTS signal, coincides with Ca^{2+} release from the glass. This would appear to be due to the cationic effusion. Governed by the Ca^{2+} rattling frequency in the glass (~12 THz)[42], this would initially outpace the polymer's ability to deform rapidly enough to bind the excess ions, being limited by the polymer's intrinsic low-frequency dynamics (~0.5 THz). Once Ca^{2+} is released from the glass, however, subsequent signal recovery over the first 1 hour traces the polymer's progressive chelation of Ca^{2+} at the interface, until Al^{3+} emerges from the glass network at ~1.5 hours, initiated by a sharp drop in reflectance continuing to ~5 hours. As the polymer is increasingly localised into a percolating matrix around the glass powder[13] and, with gel formation on the glass-particle surfaces[4,5], we would expect an associated dampening of the CTS signal, approaching the values of the isolated polymer component (Figure 2c). This drop, however, is then followed by a sharp increase in THz-reflectance, signalling increased activation of interfacial collective modes, and thus of increased coupling between polymer and alumino-silicate glass components. Accordingly, the minimum at 3 hours, we propose, defines a coupling point (CP) in the reaction-setting mechanism, after the cement has lost its initial plasticity (Figure 1d), but before it has started to establish its mechanical strength. More generally, modulation of fluctuations in the sub-THz-regime generally has been linked to elasticity and shear-induced phase transitions[43] and has also been associated with the stability of zeolite structures[44], proteins[32] and in general is typical of the librational dynamics of two-level systems in network structures[42].

Atom cohesion and fracture toughness changes. The momentum peak widths Δp_i of individual atom types *i*, measured by NCS (Supplementary Figure 3), quantify the depths of interatomic potentials, and these relate directly to atomic cohesion[34]. Marked oscillatory changes in Δp_i occur during GIC setting (Supplementary Figure 3a), particularly over the first day. In order to obtain the average momentum width Δp^{av} representative of all elements in the

setting cement, Δp_i are combined as $\Sigma_i c_i \Delta p_i$, where c_i is the element fraction. Note that Δp^{av} is bounded by $\Delta p^{polymer}$ and Δp^{glass} widths for respective polymer and glass components, measured separately (Figure 3a). As setting advances, Δp^{av} starts close to the $\Delta p^{polymer}$ width, and increases over 62 hours, levelling off below the width of the starting mixture, which is dominated by glass Δp^{glass}. During this time there is an inflection point at ~5 hours, which we have identified from CTS THz spectra as the coupling point between glass and polymer. This is followed by a clear maximum at ~8 hours, where the atomic cohesion is greatest. We define this as the initial setting point (ISP). This might be the desirable point for cementation to halt. However, there is then a minimum at ~15 hours, where atomic cohesion momentarily drops before recovering. We later identify this, from changes in $S(Q)$ (Figure 4e), as an interfacial stress zone (ISZ). Thereafter the average momentum width Δp^{av} starts to level out.

Since NCS probes atomic cohesion[34], when Δp^{av} is lower, average atomic cohesion is also lower, interatomic potentials shallower and wider and thus the material is tougher, and *vice versa*. Accordingly we expect that Δp^{av} and fracture toughness K_C might be inversely related for groups of materials. This is demonstrated in Figure 3b for the GIC system studied, where Δp^{av} values for this GIC composite measured at 24 hours are plotted, together with $\Delta p^{polymer}$, Δp^{glass} measured separately, as well as those of related compounds (see Supplementary Materials). All are plotted directly as a function of values of fracture toughness K_C reported in the literature[21,45–47]. These extend from single values for specific materials, like SiO_2 or CaF_2, to ranges of values of K_C for different systems like glasses and polymers, which span different compositions and material treatments. The asterisked values relate to the particular components, compositions and preparation protocol used in this study (Methods). The spread of the K_C values around these asterisked points for other glasses, GICs and polymer systems extend to smaller or larger values. These are smallest for oxide glasses and largest for phosphate glasses. Fracture toughness of

the GIC glass falling midrange defining the value used in Figure 3b. Compared with glasses, the span of K_C is much larger for polymers, where K_C is strongly governed by molecular weight M_n[45], which, for the polymer used for the present GIC, lies close to 22,000[7,9] and determines the asterisked value in Figure 3b. The value of M_n in turn influences the mechanical properties not just of polymers but also of GICs[48,49] In particular K_C is greater for resin-modified GICs than for conventional GICs where the current GIC system falls midway, which determines the final asterisked value. Taken together these well-defined points result in our empirical relationship between Δp^{av} and K_C being also well-defined. This is not a reciprocal relationship, as the negative slope, $d\Delta p^{av}/dK_C$, decreases with increasing K_C. Figure 3b provides a practical look-up table to calibrate Δp^{av} widths in $Å^{-1}$ measured with NCS with fracture toughness in MPa $m^{1/2}$, and is used to convert Δp^{av} from Figure 3a into average fracture toughness values K_C^{av} at 300 K during setting (Figure 3c).

Both atomic cohesion measured from Δp^{av} using NCS and fracture toughness K_C^{av} are opposite sides of the same coin and reveal the same CP, ISP and ISZ features in monotonic setting observed early on (Figure 3a,c). Moreover, K_C^{av} obtained from NCS observations offers a way to continuously access mechanical toughness *in situ*, otherwise complicated by the statistical averaging of multiple specimens inherent in retrospective destructive fracture testing[18]. In particular K_C^{av} drops sharply with setting time (Figure 3c), in line with the anticipated fall in ν (Figure 1d), followed by the coupling (CP), setting (ISP) and stress (ISZ) points. Thereafter, K_C levels out over the next 2 days, significantly above the baseline toughness – derived using the mixing ratio of the glass and polymer components' K_C values (Figure 3c). We observe similar progression in K_C^{av} at different setting temperatures over the first day (Figure 3d, Supplementary Figure 3b). These reveal expected upward shifts in temperature with time for the features CP, ISP and ISZ, as the setting temperature increases.

The elemental momentum widths Δp_i (Supplementary Figure 3a) analysed from the single particle momentum distribution (Supplementary Figure 2b) can be converted into elemental fracture toughness values K_C^i using the same empirical relationship (Figure 3b). These are shown for H, F, O and Al (Figure 3e,f) and share the same overall scale as K_C^{av} (Figure 3c), ranging from H with the highest fracture toughness values (~1.3 MPa $m^{1/2}$) to Al with the lowest (~0.3 MPa $m^{1/2}$). Elemental values can be interpreted as imparting different degrees of fracture toughness at the atomistic level, with H and Al, for example, possibly contributing toughness and brittleness respectively. The reaction points CP, ISP and ISZ are again evident. However, H, F and Al exhibit oscillatory changes in K_C^i (and Δp_i) with setting time (Figure 3e,f, Supplementary Figure 3a) which are averaged out in K_C^{av}. These may be associated with developments in hydration (K_C^H), fluorination (K_C^F), and chelation (K_C^{Al}), respectively. This sensitivity to differing chemical bonding is illustrated by hydrogen (Supplementary Figure 3a). Eventual Δp^H for GICs reported here is 4.81 $Å^{-1}$, similar to water (4.84 $Å^{-1}$), but greater than ZrH_2 (4.15 $Å^{-1}$) or NaH (3.32 $Å^{-1}$)[34,50,51].

We consider that variable H cohesion during setting has two principal staggered sources: (A) hydration of the alumino-silicate glass phase GP1 (H_2O+≡Si/Al-O-Si/Al≡ → ≡Si/Al-OH^-+-OH-Si/Al≡) binding OH^-; (B) PAA carboxylation at the interfaces (COOH ↔COO^- + H^+) freeing H^+ or H_3O^+. (A) is likely to be linked with gelation at CP, and (B) with subsequent chelation of Al at the ISP that follows at the interfaces. This is consistent with the first minima (binding of OH^-) and maxima (release of H_3O^+) in K_C^H with setting time (Figure 3e). Likewise the subsequent maximum in K_C^F corresponds to low atomic cohesion which can be associated with release of F^-. The considerable quantity of F^- in the glass substantiates reports of AlO_3F centres charge balanced by F-Ca and F-Na[36], which in G338 probably originate from both GP2

and GP3 glass phases (Figure 2a). Accordingly, we interpret oscillatory changes in K_C^F with setting time principally with the transformation of oxyfluorides into oxides at the interfaces, accompanied by the release of F^- when the atomic cohesion is least (Figure 3e). Indeed the similarity of K_C^F to K_C^{Al} (Figures 3e,f) points to F^- and Al^{3+} being partners in the same process, AlO_3F converting to AlO_4 at the ISP. The leaching of F^- during early setting provides caries resistance while actively stimulating tooth tissue remineralisation, as is often claimed in the literature[7,11,37]. It seems likely, too, that the compositional species from the Ca, F + P-rich glass phase (GP3) that assists tooth mineralisation[10] will be released during the corrosion of the glass at CP. Finally, because oxygen is involved in hydration, fluorination and chelation, we expect setting variations in K_C^O will closely follow the overall fracture toughness K_C^{av}, which indeed it appears to be the case, including the ISZ maximum close to ~15 hours (Figure 3c,f).

Atomic structure and interfacial stress. Time-averaged structure factors $S(Q)$ (where Q is the neutron scattering vector) and total radial distribution functions $G(r)$ (where r is the interatomic distance, with nearest neighbour (NN) and next nearest neighbour (NNN)) for the GIC, glass and polymer components measured separately are compared in Figure 4a,b. $S(Q)$ for the GIC and polymer include artefacts in amplitude, relating to the featureless, but substantial, incoherent scattering of hydrogen (Methods). The peak positions on Q axis in $S(Q)$ and peaks in $G(r)$, though are reliable. Deuteration was avoided in this study, because this would have adversely affected diffusion and cement-setting processes.

Both GIC and glass $S(Q)$s exhibit an initial peak – known as the first sharp diffraction peak (FSDP). This directly reflects the average length of intermediate-range order domain r_{IRO} in oxide glasses[42]. The position of the FSDP Q_{FSDP} ($2\pi/r_{IRO}$) is composition- and pressure-dependent. The fluctuating position of the FSDP (Figure 4c,d) therefore indicates changes in composition and internal stress. Q_{FSDP} for G338 glass is located between 1.5 $Å^{-1}$ for silica and

alumina-silicate glasses and 1.9 $Å^{-1}$ for phosphate glasses[42]. We therefore attribute the initial decrease in Q_{FSDP} for GIC (Figure 4d) to the release of phosphate from the Ca, F + P-rich glass phase (GP3 Figure 2a). Beyond the ISP there is a sharp increase consistent with compression developing in the remaining glass, followed by decompression, defining the start and end of ISZ. The internal pressure in the glass can be estimated by comparing the shift in Q_{FSDP} for silica with the permanent density change under pressure[52], and points to ~1 GPa being generated in the glass after the ISP at ~8 hours, then released by ~24 hours (Figure 4d).

The integrated Small-Angle Neutron Scattering (SANS) from 0.5 to 1 $Å^{-1}$ ($\int_{Q_{\min}}^{Q_{\max}} S(Q)\, Q^2 \mathrm{d}Q$) from Figure 4c is also shown in Figure 4d. SANS, which measures differential density at the nano-level, is dominated here (~0.5 $Å^{-1}$) by Porod scattering from interfaces[42], which in this case will be principally between the polymer and glass components (Figure 4c). As the major amorphous phase separation structure in the glass (GP_2) is ~50 nm in size (Figure 2a), equivalent to ~0.002 $Å^{-1}$, it is out of range for the present SANS experiments. Instead SANS intensity, which is proportional to interfacial density within the GIC, increases towards the ISZ, then drops sharply before recovering at ~24 hours; this indicates initial tension at the hybrid interfaces when the density is lowest , then stress release over the ISZ when the original density recovers (Figure 4d).

Taken together these variations in nanoscopic structure start with decreased density contrast pointing to tension at the interfaces (SANS) as the glass compresses (increase in FSDP Q_{FSDP}) constrained by the increasingly rigid surrounding matrix. This is followed by overall stress release, where density contrast at the interfaces observed from SANS and pressure from the decrease in Q_{FSDP} is restored, and suggests interfacial failure develops over the later stages of the ISZ. Indeed, indentation studies have shown that macroscopic cracks occur at GIC hybrid

interfaces[13]. Potential failure should occur via Al^{3+} linkages, as an alternative to fracture propagation at ionic sites within the polysalt complex, which has also been suggested[48], where Al^{3+} bonding may also play an important role.

In order to ascertain whether complementary changes in real-space structure occur, we have turned to time-dependent total radial distribution functions, $G(r)$s (Figure 4e). Because the hydrogen content of the polymer and GIC distorts amplitudes, conventional pair-distribution analysis was replaced by differencing out the effects of hydrogen in the setting of GIC by using $\Delta G(r)$s (Figure 4f). Furthermore, $\Delta G(r)$s also masks the unreacted glass and polymer components, highlighting changes in local atomic structure at the interfacial regions during cementation.

Separately measured $G(r)$s for GIC, glass and polymer exhibit two well-resolved peaks, due to nearest and next-nearest (atomic) neighbours, NN and NNN respectively (Figure 4b). This complex multicomponent composite includes numerous interatomic distances within the NN and NNN envelopes, related both to the polymer and glass, as well as to the organic-inorganic interfaces. Figure 4e is therefore annotated with the principal atomic pair correlations in the polymer, such as C=O and C-C, and Al-O_4, Al-O_6 and O-[Si/Al]-O in the G338 glass; as well as fluorinated environments identified spectroscopically[36], including F-Ca and F-Na. None of these can be unequivocally identified.

Measurable changes occur in $G(r)$ with setting, however, enhanced with differencing, which effectively removes unreacted components in the bulk (Figure 4e,f). Notably the coordination of interfacial Al(IV)O transforms to Al(VI)O over the ISZ, with complementary fluctuations in the carboxylate (C=O) correlations, coinciding with generation and then release of internal interfacial stress (Figure 4d,f). Additionally, the switch between Ca/Na-F and Ca/Na-O is consistent with discharge of F (Figure 3e). Both swings in nanoscopic structure – SANS and

FSDP (Figure 4d) and in atomic structure – $\Delta G(r)$ (Figure 4f), coincide with the rise and fall of toughness K_C^{av} around 15 hours (Figure 3c) and the complementary minimum in atomic cohesion (Figure 3a).

Discussion

Comparatively few materials have been measured to date using Neutron Compton Scattering (NCS) – GICs being the first complex and dynamic system to be studied. Necessarily, there are differences in NCS profiles with temperature, pressure and inter-atomic bonding, the latter having provided the avenue to track changing atomic cohesion and dynamic interfacial configurations during cementation. Comparisons between elemental NCS peak widths Δp_i (Supplementary Figure 3a) and overall Δp (Supplementary Figure 3b) and Fracture Toughness therefore need to relate to the specific materials studied – glass, GIC or polymer – and for them to be measured under the same conditions.

Such geometric switching, mainly dynamic configurations of Al ranging from 4-coordinated tetrahedra originating in the glass, to 5-coordinate pyramidal, is the likely initial GIC-setting sequence between CP and the Initial Setting Point (ISP). The coherent THz frequencies detected at the developing hybrid interface are in the collective mode range, comprised of twisting, rocking, flexing and compressing modes – potentially at flexural Al-pivots. Importantly these fall among the collective modes reported for SiO_2[44], inorganic glasses and zeolite structures[44], and typical of the dynamics of two level systems[42].

The successful juxtaposition of *in situ* sub-THz spectroscopy and neutron methods with DSC herein has enabled the complex setting-reaction processes of GIC dental composites to be unravelled structurally, energetically and dynamically at the atomic level for the first time. Our

methods are equally applicable to studying fracture-toughness development in modified bioactive cement compositions[53], where setting may be faster or slower, or in resin-modified GICs before and after curing, including the collective THz-dynamics, which, in turn, are linked to inter-particle and interfacial dynamics. We expect that this battery of techniques will also offer advantages more generally for studying mechanical toughness microscopically and non-destructively in other types of mercury-free cements during setting.

Methods

Materials. The composition of the G338 glass powder, (First Scientific Dental GmbH, Elmsohm, Germany) was $Na_{6.3}Ca_{6.6}P_{6.2}Al_{16.9}Si_{11.8}O_{32.5}F_{19.7}$[7] and was hand-mixed with Chemflex liquid (Dentsply DeTrey GmbH, Germany) of 40% polyacrylic acid solution, in a respective 2.5:1 ratio for all experiments (Figure 1b), the proportions leaving the aqueous polymer fraction above the percolation threshold (16%), ensuring that glass particles were fully enveloped. Fresh cement was promptly loaded into measurement canisters. Setting time was recorded from the start of mixing. In each case the powder and polymer were similarly measured separately, the 2.5:1 ratio providing the baseline $t = 0$ values (Figure 3a,c).

Transmission Electron Microscopy. TEM was performed at the NanoVision Centre at QMUL using SEM and TEM facilities. The G338 glass powder was dried before mounting. With an average particle size range of ~4 μm (Supplementary Figure 4), many smaller fragments ~1 μm were also imaged, revealing phase separation of 50 nm rosette globules within a matrix (Figure 2a).

Differential Scanning Calorimetry. The isobaric heat capacity (C_p) data for both G338 and the GIC sample subjected to the 62 hours setting and subsequent first DSC up- and down scans

(Figure 2b) were collected in an argon atmosphere using a Netzsche STA449C; reproducibility being checked for baseline drift. G338 underwent 2 runs of up- and downscan (see glass 338 upscan-1 and upscan-2 curves). For scan 1 the sample was held for 5 min at 323 K, heated at 20 K min^{-1} to 873 K, and then cooled back to 523 K at 20 K min^{-1}. Scan 2 followed the same procedure. C_p was determined using a sapphire reference.

Supplementary Figure 1 shows two upscan curves for both the DSC output (isobaric heat capacity Cp) and the mass change of the GIC sample which was subjected to a 62 hours setting. The sample was upscanned in argon at 20 K min^{-1}. The first upscan curve in Supplementary Figure 1a displays two endothermic responses indicating the water evaporation between 340 and 600 K, and the PAA decomposition between 600 and 800 K. These two thermal responses are reflected in the 2-stage drop in mass as shown in Supplementary Figure 1b.

Coherent Terahertz spectroscopy. Spectra of G338, Chemflex and the setting cement (Figure 2c) were obtained using a unique coherent THz transceiver[33] incorporating vector-network-analyser-driven quasi-optical circuitry (Supplementary Figure 5). The cement was loaded into a THz-transparent (polyethylene) vessel (Supplementary Figure 6) and set at the focal-point of fast-mirrors, F2 and sealed to maintain water content. The sample absorbance was recorded as spectral reflectance response relative to a standard flat aluminium reflector.

Neutron Compton scattering. NCS spectra were obtained using VESUVIO spectrometer at the ISIS neutron source, with sample sizes of 55g glass, 20g polymer and 14 g cements (10g glass + 4g polymer – to give 2.5:1 mix ratios), and repeated at differing temperatures (280K, 300K, 320K). Under the conditions of high neutron energy transfer, 1 eV to 30 eV, and wave-vector transfer, 30 $Å^{-1}$ to 200 $Å^{-1}$, the Impulse Approximation is valid[34]. This treats the neutron scattering event as involving a single atom, with conservation of the total kinetic energy and

momentum of the neutron plus the atom. NCS therefore probes the momentum distribution $n_i(p)$ of each element *i* present in the sample.

Calibration was first done by measuring the empty beam and the empty sample holder. The empty sample holder spectrum and the multiple scattering were always subtracted before any data analyses. Multiple scattering was calculated using the assessed Monte Carlo code DINSMS[54], which is routinely used for multiple scattering determinations for NCS experiments. In particular the code calculates the time of flight spectrum of multiply scattered neutrons from samples of known geometry and compositions in DINS experiments. Such a contribution can be isolated in the simulation and subtracted from the experimental data; a detailed description can be found in Ref .(54). The raw time-of-flight data for each single detector spectrum were fitted using the known stoichiometry of the sample. The fitting was carried out after correction for multiple scattering and subtraction of the sample canister signal. Examples are shown in Supplementary Figure 2 for forward and backward geometries. These include fitting to NCS momentum widths Δp_i for GIC elements present as shown, taking advantage of the instrument's ability to probe single particle momentum distribution[55,56]. The individual element-specific time-of-flight data were then transferred to momentum space, and then the peak width of each element Δp_i was calculated in $Å^{-1}$ as FWHM (Supplementary Figure 3), following existing procedures[34]. Also included is the difference between adjacent time slices close to the ISZ (Figure 3c). The setting dependent elemental momentum widths Δp^H, Δp^F, Δp^O and Δp^{Al} used to create the mechanical fracture toughness plots in Figure 4e,f are shown in Supplementary Figure 3a and exhibit significant variations with setting time. The overall average momentum widths ($\Sigma_i c_i \Delta p_i$ where c_i is the elemental atomic fraction) for setting at 280 K, 300 K and 320 K, $\Delta p^{280\ K}$, $\Delta p^{300\ K}$, $\Delta p^{320\ K}$, from which K_C^{av} plots in Figure 3d were obtained, are plotted in Supplementary Figure 3b.

Neutron diffraction. Data were collected using NIMROD at ISIS[35]. Calibration was done using a vanadium reference, after which glass powder and liquid were measured in a TiZr cell. Setting GIC measurements were performed over 24 hrs. Data were analysed using the Gudrun program package[57] to correct for the contributions from the empty cell, instrument background and to normalise the data to absolute units using the scattering of a vanadium standard absorption before attenuation and multiple-scattering corrections. Correction for the contribution from inelastic scattering by the sample was made using a well-established method[58], incorporating equations developed for total-scattering correlation functions to provide consistent definitions[59].

The total-scattering structure factor $F(Q)$ measured in the absolute units of barn per steradian per atom is defined as follows:

$$F(Q) = \sum_{\alpha \leq \beta} (2 - \delta_{\alpha\beta}) c_\alpha c_\beta b_\alpha b_\beta [A_{\alpha\beta}(Q) - 1]$$

Where c_α and c_β are the concentrations of atom type α and β; b_α and b_β are their corresponding neutron scattering lengths; $\delta_{\alpha\beta}$ is the Kronecker delta function to avoid double counting interactions between like-atom pairs; $A\alpha_\beta(Q)$ are the Faber–Ziman partial structure factors.

Structure factor $S(Q)$ was obtained by normalising $F(Q)$:

$$S(Q) = 1 + \frac{F(Q)}{(\sum_\alpha c_\alpha b_\alpha)^2}$$

Where $\sum_\alpha c_\alpha b_\alpha$ is material scattering length.

There is a negative swing at low-Q region in polymer $S(Q)$ in Figure 4a. This is because the scattering length of the polymer is very small, due to the negative incoherent scattering length of H, which then amplifies the negative peak in the low-Q region of $F(Q)$ during normalisation. This negative swing is thus not shown in Figure 4a. This anomaly can be avoided if deuterated

specimens are used but was avoided in this study because of its affect on the dynamics of the setting process.

And the total radial distribution function $G(r)$ is obtained by the direct Fourier transform of $F(Q)$:

$$G(r) = \frac{1}{(2\pi)^3 \rho} \int_0^\infty 4\pi Q^2 F(Q) \frac{\sin(Qr)}{Qr} dQ$$

where ρ is the atomic density of the material.

As the samples are sealed during measurements, trends in $S(Q)$ and $G(r)$ for the polymer are consistent with a fixed hydrogen content. Due to the effect of high hydrogen content of the GIC conventional pair-distribution analysis of $G(r)$ was replaced by differencing (Figure 4f).

References

1. United Nations Environment Programme (UNEP) (2013), The Global Mercury Assessment 2013: Sources, Emissions, Releases and Environmental Transport. UNEP Chemicals Branch, Geneva, Switzerland.

2. BIO Intelligence Service (2012), Study on the potential for reducing mercury pollution from dental amalgam and batteries, Final report prepared for the European Commission - DG ENV.

3. Wilson, A. D. & Kent, B. E. A new translucent cement for dentistry. The glass ionomer cement. *Br. Dent. J.* **15,** 133–135 (1972).

4. Crisp, S. & Wilson, A. D. Reactions in glass ionomer cements: I. Decomposition of the powder. *J. Dent. Res.* **53,** 1408–1413 (1974).

5. Crisp, S. & Wilson, A. D. Reactions in glass ionomer cements: II. An infrared spectroscopic study. *J. Dent. Res.* **53,** 1414–1419 (1974).

6. McLean, J. W. & Wilson, A. D. The clinical development of the glass-ionomer cement. II. Some clinical applications. *Aus. Dent. J.* **22,** 120–127 (1977).

7. Nicholson, J. W. Chemistry of glass-ionomer cements: a review. *Biomater.* **19,** 485–494 (1998).

8. Davidson, C. L. Advances in glass-ionomer cements. *J. Appl. Oral. Sci.* **14,** 3–9 (2006).

9. International Standard Organization (1986). Specification 7489. Dental glass polyalkenoate cements.

10. Atmeh, A. R., Chong, E. Z., Richard, G., Festy, F. & Watson, T. F. Dentin-cement interfacial interaction: calcium silicates and polyalkenoates. *J. Dent. Res*. **91,** 454–459 (2012).

11. Ten Cate, J. M. & van Duinen, R. N. B. Hypermineralization of dentinal lesions adjacent to glass-ionomer cement restorations. *J. Dent. Res*. **74,** 1266–1271 (1995).

12. Lloyd, C. H. & Mitchell, L. The fracture toughness of tooth coloured restorative materials. *J. Oral. Rehabil*. **11,** 257–272 (1984).

13. Tian, K. V., *et al.* Qualitative assessment of microstructure and Hertzian indentation failure in biocompatible glass ionomer cements. *J. Mater. Sci. Mater. Med*. **23,** 677–685 (2012).

14. Kovarik, R. E., Haubenreich, J. E. & Gore, D. Glass ionomer cements: a review of composition, chemistry, and biocompatibility as a dental and medical implant material. *J. Long Term Eff. Med. Implants* **15,** 655–671 (2005).

15. Jonck, L. M., Grobbelaar, C. J. & Strating, H. Biological evaluation of glass-ionomer cement (Ketac-0) as an interface material in total joint replacement. A screening test. *Clin. Mater*. **4,** 201–224 (1989).

16. Bauer, M., Pytel, J., Vona, I. & Gerlinger, I. Combination of ionomer cement and bone graft for ossicular reconstruction. *Eur. Arch. Otorhinolaryngology* **264,** 1267–1273 (2007).

17. Hatton, P.V., Hurrell-Gillingham, K. & Brook, I. M. Biocompatibility of glass-ionomer bone cements. *J. Dent.* **34,** 598**–**601 (2006).

18. Hertzberg, R. W., Vinci, R. P. & Hertzberg, J. L. *Deformation and Fracture Mechanics of Engineering Materials* (Wiley, 5th edition, 2012).

19. Ashby, M. *Materials Selection in Mechanical Design* (Burlington, Massachusetts: Butterworth-Heinemann, 3rd Edition, 1999).

20. Ritchie, R. O. The conflicts between strength and toughness. *Nat. Mater.* **10,** 817–822 (2011).

21. Wondraczek, L., *et al.* Towards ultrastrong glasses. *Adv. Mater.* **23,** 4578–4586 (2011).

22. Greaves, G. N., Greer, A. L., Lakes, R. S. & Rouxel, T. Poisson's ratio and modern materials. *Nat. Mater.* **10,** 823–837 (2011).

23. Fracture energy G_C is related to fracture toughness K_C by $G_C = K_C^2(1-\nu^2)/E$, where E is Young's modulus and ν is Poisson's ratio.

24. Lewandowski, J. J., Wang, W. H. & Greer, A. L. Intrinsic plasticity or brittleness of metallic glasses. *Phil. Mag. Lett*. **85,** 77–87 (2005).

25. Akinmade, A. O. & Nicholson, J. W. Poisson's ratio of glass-polyalkenoate ("glass-ionomer") cements determined by an ultrasonic pulse method. *J. Mater. Sci. Mater. Med.* **6,** 483–485 (1995).

26. Greaves, G. N., *et al*. Glancing-angle x-ray absorption spectroscopy of corroded borosilicate glass surfaces containing uranium. *J. Am. Chem. Soc.* **111,** 4313–4324 (1989).

27. Xue, X. Y. & Kanzaki, M. Al coordination and water speciation in hydrous aluminosilicate glasses: direct evidence from high-resolution heteronuclear ^{1}H-^{27}Al correlation NMR. *Solid State Nucl. Magn. Reson.* **31,** 10–27 (2007).

28. Zainuddin, N., Karpukhina, N., Hill, R. G. & Law, R. V. A long-term study on the setting reaction of glass ionomer cements by ^{27}Al MAS-NMR spectroscopy. *Dent. Mater.* **25,** 290–295 (2009).

29. Acbas, G., Niessen, K. A., Snell, E. H. & Markelz, A. G. Optical measurements of long-range protein vibrations. *Nat. Commun*. **5,** 3076 (2014).

30. Averett, D., Cicerone, M. T., Douglas J. F. & de Pablo J. J. Fast relaxation and elasticity-related properties of trehalose-glycerol mixtures. *Soft Matter* **8,** 4936–4945 (2012).

31. Hu, W., *et al*. Optically enhanced coherent transport in $YBa_2Cu_3O_{6.5}$ by ultrafast redistribution of interlayer coupling. *Nat. Mater*. **13,** 705–711 (2014).

32. Grossman, M., *et al*. Correlated structural kinetics and retarded solvent dynamics at the metalloprotease active site. *Nat. Struct. Mol. Biol.* **18,** 1102–1108 (2011).

33. McIntosh, A. I., Yang, B., Goldup, S. M., Watkinson, M. & Donnan, R. S. Terahertz spectroscopy: a powerful new tool for the chemical sciences? *Chem. Soc. Rev*. **41,** 2072–2082 (2012).

34. Mayers, J. Quantum effects in deep inelastic neutron scattering. *Phys. Rev. B* **41,** 41–51 (1990).

35. Bowron, D. T., *et al*. NIMROD: the Near and InterMediate Range Order Diffractometer of the ISIS second target station. *Rev. Sci. Instru.* **81,** 033905 (2010).

36. Stamboulis, A., Law, R. V. & Hill, R. G. Characterisation of commercial ionomer cements using magic angle nuclear magnetic resonance (MAS-NMR). *Biomater.* **25,** 3907–3913 (2004).

37. Hill, R. G. & Wood, D. Apatite-mullite glass ceramics. *J. Mater. Sci. Mater. Med.* **6,** 311–318 (1995).

38. James, P. F. in *Glasses and Glass-Ceramics*, edited by Lewis, M. H. (London: Chapman and Hall. 1989).

39. Wasson, E. A. & Nicholson, J. W. A study of the relationship between setting chemistry and properties of modified glass polyalkenoate cements. *Brit. Polym. J.* **23,** 179–183 (1990).
40. Pedersen, M. T., *et al.* Phase separation in an ionomer glass: insight from calorimetry and phase transitions. *J. Non-Cryst. Solids* **415**, 24–29 (2015).
41. Yue, Y. Z. & Angell, C. A. Clarifying the glass-transition behaviour of water by comparison with hyperquenched inorganic glasses. *Nature* **427,** 717–720 (2004).
42. Greaves, G. N. & Sen, S. Inorganic glasses, glass-forming liquids and amorphizing solids. *Adv. Phys.* **56,** 1–166 (2007).
43. Ryder, M. R., Civalleri, B., Bennett, T. D., Henke, S. & Rudić, S. Identifying the role of terahertz vibrations in metal-organic frameworks: from gate-opening phenomenon to shear-driven structural destabilization. *Phys. Rev. Lett*. **113,** 215502 (2014).
44. Greaves, G. N., Meneau, F., Majérus, O., Jones, D. G. & Taylor, J. Identifying the vibrations that destabilize crystals and characterizes the glassy state. *Science* **308,** 1299–1302 (2005).
45. Prentice, P. The influence of molecular weight on the fracture of glassy polymers. *J. Mater. Sci.* **20,** 1445–1454 (1985).
46. Goldman, M. Fracture properties of composite and glass ionomer dental restorative materials. *J. Biomed. Mater. Res.* **19,** 771–783 (1985).
47. Lloyd, C. H. & Adamson, M. The development of fracture toughness and fracture strength in posterior restorative materials. *Dent. Mater.* **3,** 225–231 (1987).
48. Hill, R. G., Wilson, A. D. & Warrens, C. P. The influence of poly(acrylic acid) molecular weight on the fracture toughness of glass-ionomer cements, *J. Mater. Sci.* **24,** 363–371 (1989).
49. Griffin, S. & Hill, R. Influence of poly(acrylic acid) molar mass on the fracture properties of glass polyalkenoate cements. *J. Mater Sci*. **33,** 5383–5396 (1998).
50. Seel, A. G., Sartbaeva, A., Mayers, J., Ramirez-Cuesta, A. J. & Edwards, P. P. Neutron Compton scattering investigation of sodium hydride: From bulk material to encapsulated nanoparticulates in amorphous silica gel. *J. Chem. Phys*. **134,** 114511 (2011).
51. Mayers, J. & Reiter, G. The VESUVIO electron volt neutron spectrometer. *Meas. Sci. Techol.* **23,** 045902 (2012).
52. M. Zanatta, M., et al. Structural evolution and medium range order in permanently densified vitreous SiO_2, *Phys. Rev. Lett.* **112**, 045501 (2014).
53. Moshaverinia, A., Roohpour, N., Chee, W. W. L. & Schricker, S. R. A review of powder modifications in conventional glass-ionomer dental cements. *J. Mater. Chem.* **21,** 1319–1328 (2011).

54. Mayers, J., Fielding, A. L. & Senesi, R. Multiple scattering in deep inelastic neutron scattering: Monte Carlo simulations and experiments at the ISIS eVS inverse geometry spectrometer. *Nucl. Instr. Meth. Phys. Rev. A* **481,** 454–463 (2002).

55. Krzystyniak, M., Richards, S. E., Seel, A. G. & Fernandez-Alonso, F. Mass-selective neutron spectroscopy of lithium hydride and deuteride: Experimental assessment of the harmonic and impulse approximations. *Phys. Rev. B* **88,** 184304 (2013)

56. Romanelli, G., et al. Direct measurement of competing quantum effects on the kinetic energy of heavy water upon melting. *J. Phys. Chem. Lett*. **4,** 3251–3256 (2013).

57. Soper, A. K. GudrunN and GudrunX: programs for correcting raw neutron and X-ray diffraction data to differential scattering cross section. Rutherford Appleton Laboratory Technical report: RAL-TR-2011-013. https://epubs.stfc.ac.uk/work/56240 (2011)

58. Soper, A. K. The radial distribution functions of water as derived from radiation total scattering experiments: is there anything we can say for sure? ISRN *Phys. Chem.* **2013,** 279463 (2013).

59. Keen, D. A. A comparison of various commonly used correlation functions for describing total scattering. *J. Appl. Cryst*. **34,** 172–177 (2001).

60. Roberts, J. C., Powers, J. M. & Craig, R. G. Fracture toughness and critical strain energy release rate of dental amalgam. *J. Mater. Sci.* **13,** 965–971 (1978).

61. Kinney, J. H., Marshall, S. J. & Marshall, G. W. The mechanical properties of human dentin: a critical review and re-evaluation of the dental literature. *Crit. Rev. Oral Biol. Med.* **14,** 13–29 (2003).

62. Toparli, M. & Koksal, N. S. Hardness and yield strength of dentin from simulated nanoindentation tests. *Comput. Meth. Prog. Biomed.* **77,** 253–257 (2005).

Acknowledgements

We acknowledge support of the neutron experiments from ISIS Pulsed Neutron & Muon facility (Science & Technology Facilities Council, UK). J. Khaliq is thanked for the TEM imaging and A. I. McIntosh for preliminary THz test runs. D. Setiadi, F. Fernandez-Alonso, A. Seel, A. Taylor, C. Andreani and R. Senesi are thanked for helpful discussions. Z. Zhou and W. Chen for graphics visualisation. K.V.T & C.D.N are grateful for financial support from the TÁMOP-4.2.1/B-09/1/KMR-2010-0001_Hungary, G.A.C & D.C.F to the Royal Society (IE20096),

G.A.C to the Engineering and Physical Sciences Research Council (EP/H030077/1, EP/H030077/2), and G.N.G to Sidney Sussex College, Cambridge (Visiting Fellowship) and Wuhan University of Technology (Strategic Scientist).

Author contributions

G.A.C carried out TEM measurements; Y.Z.Y, K.V.T and G.N.G conducted the DSC characterizations and analysed the data with G.A.C. B.Y, R.S.D and G.A.C carried out the THz measurements and analysed data with K.V.T and D.C.F. K.V.T, J.M and G.A.C performed the NCS experiments and data analysis, C.D.N and J.W.N also participated in the experiments and G.N.G was involved in the data analysis; K.V.T, D.T.B, G.A.C and G.N.G did neutron diffraction measurements and data analysis together with A.L.G was involved in the data analysis; K.V.T, G.A.C, G.N.G and assembled the figures and wrote the manuscript with A.L.G. providing editorial assistance, and Y.Z.Y. involved with sections related to DSC.

Additional information

Supplementary Information accompanies this paper at …

Competing financial interests: The authors declare no competing financial interests.

Reprints and permissions information is available at g.chass@qmul.ac.uk and

gng25@cam.ac.uk

a

b

Fig 1

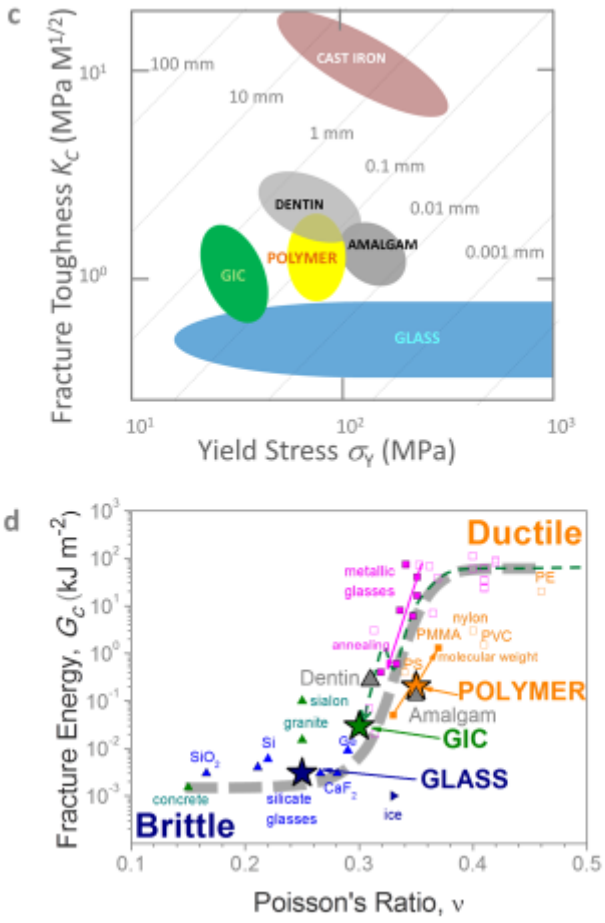
c
Fracture Toughness K_c (MPa M$^{1/2}$)
Yield Stress σ_y (MPa)
100 mm
10 mm
1 mm
0.1 mm
0.01 mm
0.001 mm
CAST IRON
DENTIN
AMALGAM
POLYMER
GIC
GLASS
d
Fracture Energy, G_c (kJ m^{-2})
Poisson's Ratio, ν
Ductile
Brittle
metallic glasses
PE
nylon
PMMA
PVC
annealing
molecular weight
Dentin
POLYMER
sialon
Amalgam
granite
GIC
Si
SiO_2
GLASS
CaF_2
concrete
silicate glasses
ice

Fig 1

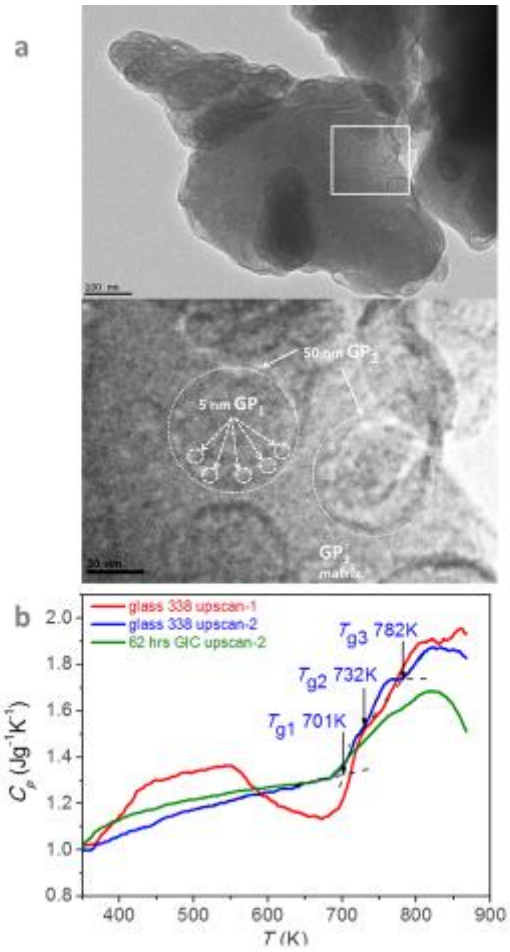
a
50 nm GP2
5 nm GP1
GP2 matrix
b
glass 338 upscan-1
glass 338 upscan-2
62 hrs GIC upscan-2
Tg3 782K
Tg2 732K
Tg1 701K
Cp (Jg-1K-1)
T (K)

Fig 2

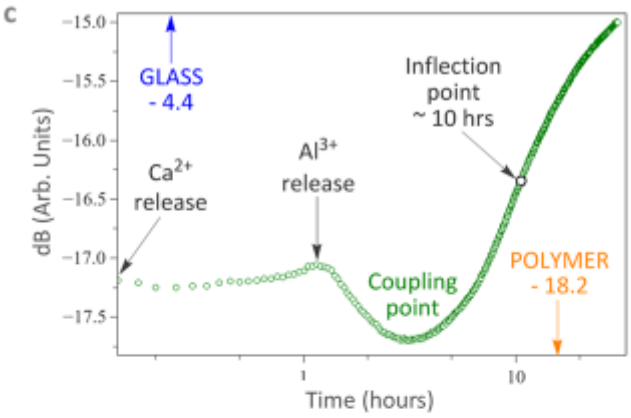
c
GLASS
- 4.4
Ca2+
release
Al3+
release
Inflection
point
~ 10 hrs
Coupling
point
POLYMER
- 18.2
dB (Arb. Units)
Time (hours)
−15.0
−15.5
−16.0
−16.5
−17.0
−17.5
1
10

Fig 2

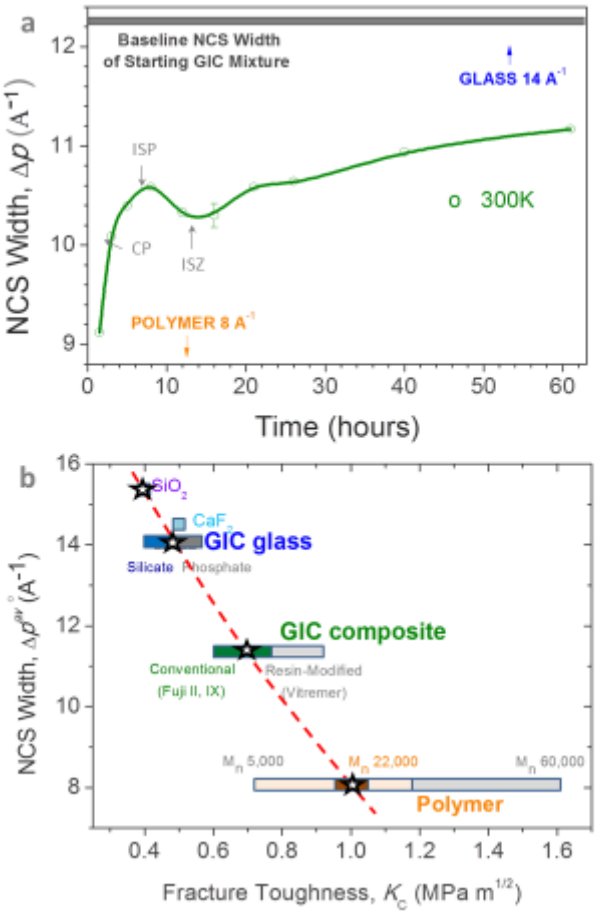
a
Baseline NCS Width
of Starting GIC Mixture
GLASS 14 A-1
ISP
CP
ISZ
o 300K
POLYMER 8 A-1
NCS Width, Δρ (A-1)
Time (hours)
b
SiO2
CaF2
GIC glass
Silicate
Phosphate
GIC composite
Conventional
(Fuji II, IX)
Resin-Modified
(Vitremer)
Mn 5,000
Mn 22,000
Mn 60,000
Polymer
NCS Width, Δρ'' (A-1)
Fracture Toughness, KC (MPa m1/2)

Fig 3

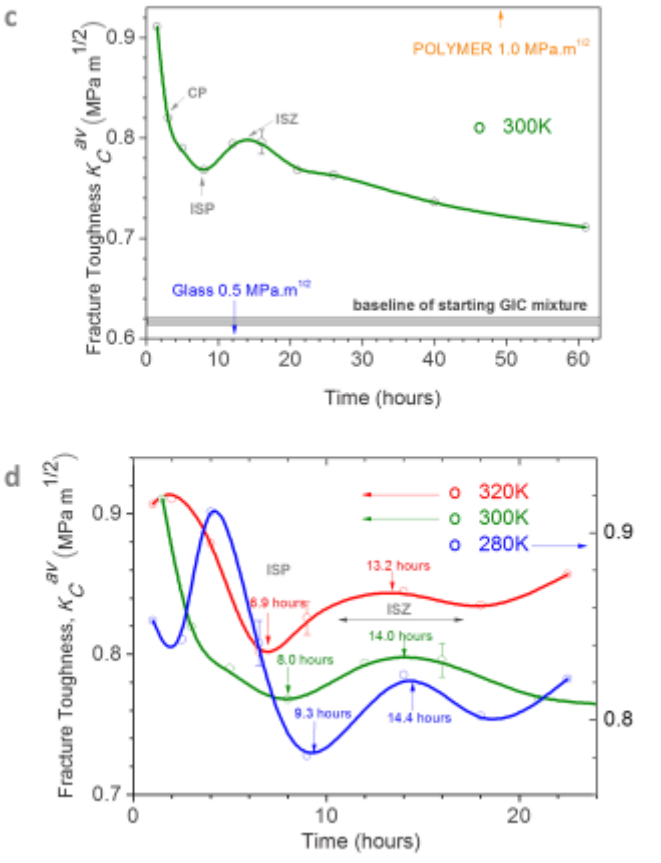
c
Fracture Toughness K_C^{av} (MPa m$^{1/2}$)
POLYMER 1.0 MPa.m$^{1/2}$
CP
ISZ
ISP
o 300K
Glass 0.5 MPa.m$^{1/2}$
baseline of starting GIC mixture
Time (hours)
d
Fracture Toughness, K_C^{av} (MPa m$^{1/2}$)
o 320K
o 300K
o 280K
ISP
13.2 hours
8.9 hours
ISZ
14.0 hours
8.0 hours
9.3 hours
14.4 hours
Time (hours)

Fig 3

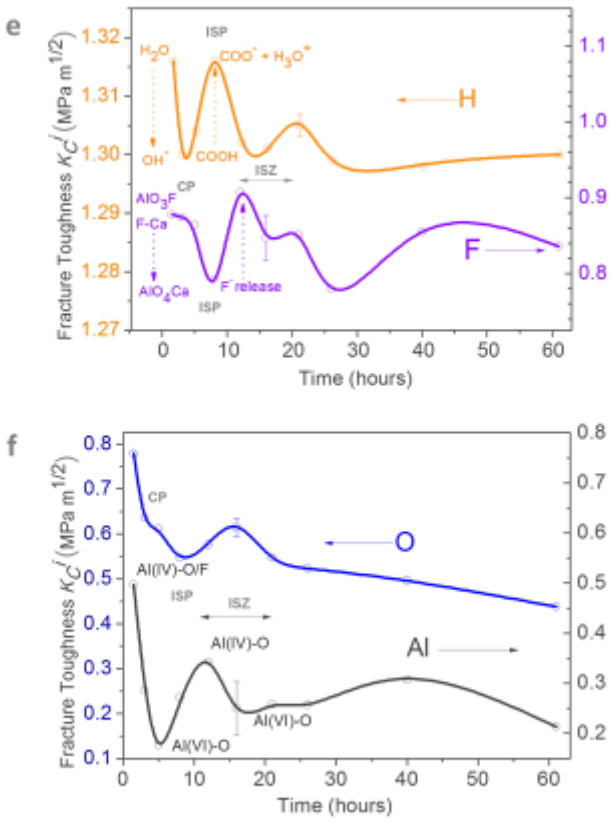
e
Fracture Toughness K_C / (MPa m$^{1/2}$)
Time (hours)
ISP
H_2O
OH^-
$COO^- + H_3O^+$
COOH
H
ISZ
CP
AlO_3F
F-Ca
AlO_4Ca
F^- release
ISP
F
f
Fracture Toughness K_C / (MPa m$^{1/2}$)
Time (hours)
CP
Al(IV)-O/F
ISP
ISZ
Al(IV)-O
Al(VI)-O
Al(VI)-O
O
Al

Fig 3

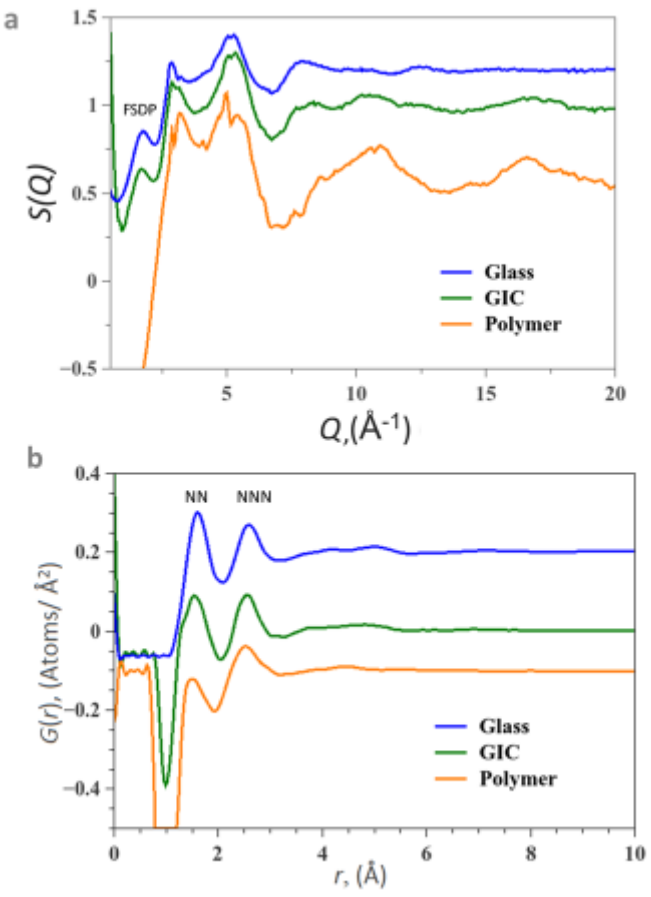
a
1.5
1
0.5
0
−0.5
S(Q)
FSDP
Glass
GIC
Polymer
5
10
15
20
Q,(Å-1)
b
0.4
0.2
0
−0.2
−0.4
G(r), (Atoms/ Å2)
NN
NNN
Glass
GIC
Polymer
0
2
4
6
8
10
r, (Å)

Fig 4

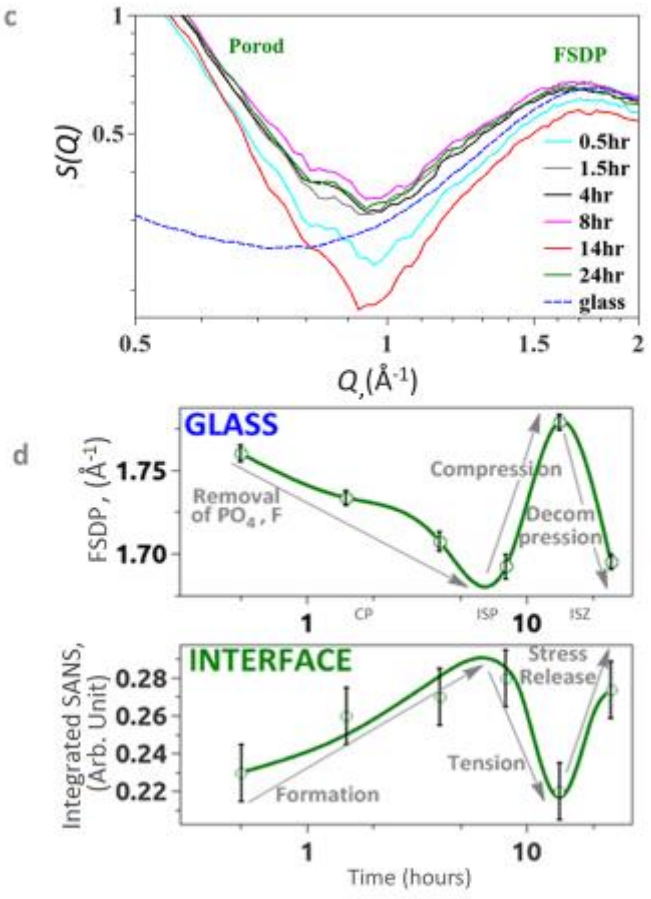
c
Porod
FSDP
S(Q)
0.5hr
1.5hr
4hr
8hr
14hr
24hr
glass
Q, (Å-1)
d
GLASS
FSDP , (Å-1)
Removal of PO4 , F
Compression
Decompression
CP
ISP
ISZ
INTERFACE
Integrated SANS, (Arb. Unit)
Stress Release
Tension
Formation
Time (hours)

Fig 4

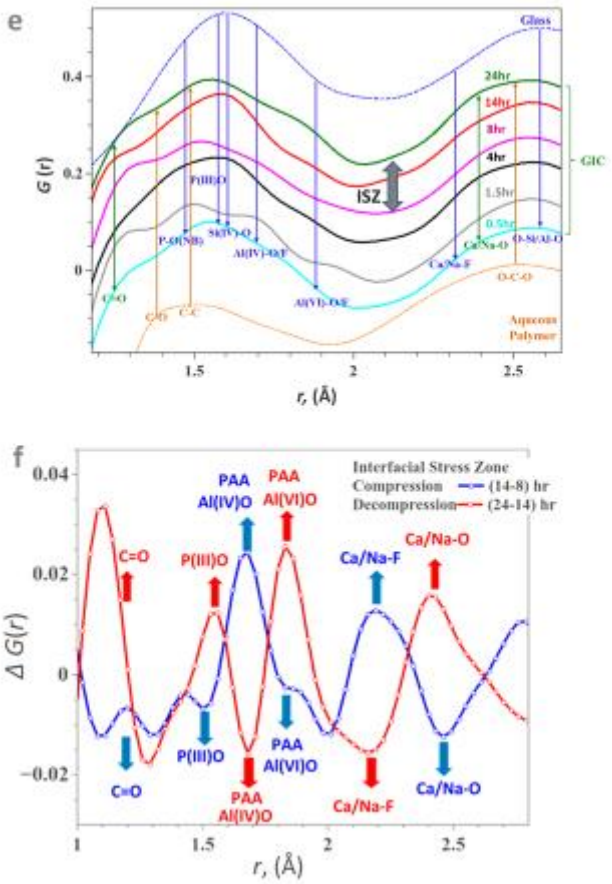
e
Glass
24hr
14hr
8hr
4hr
1.5hr
0.5hr
GIC
ISZ
G (r)
r, (Å)
Aqueous Polymer
f
Interfacial Stress Zone
Compression (14-8) hr
Decompression (24-14) hr
PAA Al(IV)O
PAA Al(VI)O
C=O
P(III)O
Ca/Na-F
Ca/Na-O
Δ G(r)
r, (Å)

Fig 4

Figure legends:

Figure 1 | GICs, mechanical properties, setting, and glass nanoscopic structure. a, GIC restorative, including occlusal view. **b**, G338 fluoro-alumino-silicate glass powder and dangling aqueous polymer (acrylic acid). **c**, Fracture toughness K_C versus strength σ_F for dental materials compiled as an Ashby plot[19]: dentin, glass and polymers[20,21,45], GICs[46,47] and amalgam[60]. **d**, Fracture energy G_c versus Poisson's ratio ν and the brittle-ductile transition[22], expanded for a wide range of materials; ν values for dental materials[25,61,62] combined with G_C values[20–22,24,45–47,60,61]; toughness decline during setting indicated by the dashed arrow; trends for annealing and polymerisation (solid arrows). **a** and **b** courtesy Faculty of Dentistry, Semmelweis University.

Figure 2 | Glass nanoscopic structure, rheology and *in situ* THz dynamics of GIC. a, TEM image of individual glass particle (above, scale bar is 100 nm) with three distinguishable glass phases: GP1, GP2 and GP3 seen on an expansion of the white frame area (below, scale bar is 20 nm, see text for details). **b**, Three DSC upscan curves for the fresh G338 glass (red), the G338 glass subjected to the first up- and downscans (blue), and the GIC sample (green) subjected to 62 hrs setting and the subsequent up- and downscans, respectively. The red curve exhibits a water-loss endothermic response, followed by an exothermic enthalpy-release response; the blue upscan-2 curve reveals three sharp glass transitions T_{g1}, T_{g2}, and T_{g3} which we associate with the glass phases GP1, GP2 and GP3 respectively; the green curve reveals how glass transitions are modified by setting. Both up- and downscan rates are 20 K min^{-1}. **c**, Coherent terahertz spectroscopy: Changing sub-THz relative reflectance during setting, differentiating gel formation (Ca^{+2} release) from chelation (Al^{+3} release); minimum (CP) identifies the point where glass and polymer couple dynamically.

Figure 3 | Non-monotonic advancement in atom cohesion and fracture toughness during GIC solidification. a, Overall GIC NCS peak width Δp^{av} variations with setting time, measuring different stages in atomic cohesion during setting: CP, ISP and ISZ (see text for details). **b**, Inverse relationship between atomic cohesion Δp^{av} and fracture toughness K_C^{av} of GIC, polymer and glass (asterisks) and associated materials (see text for details). **c**, Non-monotonic fall in overall K_C^{av} with setting time at 300 K obtained from overall Δp^{av} (**a**) using **b**, identifying CP and reaction points ISP and ISZ. **d,** K_C^{av}(280 K), K_C^{av}(300 K), and K_C^{av}(320 K), showing shifts in ISP and ISZ with setting temperature. **e**, Fluctuations in K_C^{i} for H and F, showing evidence for hydration and fluorination. **f**, K_C^{i} for O and Al through the various setting stages. Elemental fracture toughness K_C^{i} were derived from Δp_i values (Supplementary Figure 3a), with K_C^{av} (280 K, 300 K, 320 K) obtained from Δp^{av} (280 K, 300 K, 320 K) values (Supplementary Figure 3b), in each case using (**b**).

Figure 4 | Neutron scattering measurements for GIC, glass and polymer. Time-averaged **a**, $S(Q)$ and **b**, $G(r)$, including FSDP and expected locations for nearest and next-nearest-neighbour pair correlations NN and NNN respectively. **c**, *In situ* time-resolved $S(Q)$ over 24 hours revealing changes in small angle Porod scattering (SANS) at interfaces, and in the position of FSDP for the glass. **d**, Fluctuations with setting in the FSDP position and the integrated SANS from **c** (Methods). Abrupt changes around 15 hours coincide with the Δp^{av} minimum and K_C^{av} maximum (Figure 4a,c). **e**, *In situ* time-resolved $G(r)$ with NN distances for GIC related to glass (upper) and aqueous polymer (lower). **f,** Trends in $\Delta G(r)$ obtained by differencing $G(r)$ across the ISZ (from **d**) – splines for guiding the eye. **a, b** and **e** data are all offset vertically for clarity of presentation.